

1 **A lithofacies approach for modeling non-Fickian solute transport in a**  
2 **heterogeneous alluvial aquifer**

3  
4

5 Marco Bianchi<sup>1</sup>, Chunmiao Zheng<sup>2,3</sup>

6

7 <sup>1</sup> British Geological Survey, Environmental Science Centre, Keyworth, Nottingham,  
8 United Kingdom.

9

10 <sup>2</sup> School of Environmental Science and Engineering, South University of Science and  
11 Technology of China, Shenzhen, China.

12 <sup>3</sup> Department of Geological Sciences, University of Alabama, Tuscaloosa, AL, United  
13 States.

14

15

16

17

18

19

20

21 Corresponding Author:

22 Marco Bianchi, British Geological Survey, Environmental Science Centre, Keyworth,  
23 Nottingham, NG12 5GG, United Kingdom. [marcob@bgs.ac.uk](mailto:marcob@bgs.ac.uk). Tel. +44 (0)155 9363136

24

25 **Key points:**

- 26 - Lithofacies are mapped as basis for 3D hydraulic conductivity distribution.
- 27 - Non-Fickian transport behavior emerges naturally from lithofacies distribution.
- 28 - Verifiable explanations are developed for the plume behavior at the MADE site.

29

30 **Abstract.** Stochastic realizations of lithofacies assemblage based on lithological data  
31 from a relatively small number of boreholes were used to simulate solute transport at the  
32 well-known Macrodispersion Experiment (MADE) site in Mississippi (USA). With sharp  
33 vertical contrasts and lateral connectivity explicitly accounted for in the corresponding  
34 hydraulic conductivity fields, experimental results from a large-scale tracer experiment  
35 were adequately reproduced with a relatively simple model based on advection and local  
36 dispersion. The geologically based model of physical heterogeneity shows that one well  
37 interconnected lithofacies, with a significantly higher hydraulic conductivity and  
38 accounting for 12% of the total aquifer volume, may be responsible for the observed non-  
39 Fickian transport behavior indicated by the asymmetric shape of the plumes and by  
40 variations of the dispersion rate in both space and time. This analysis provides a  
41 lithological basis to the hypothesis that transport at MADE site is controlled by a network  
42 of high-conductivity sediments embedded in a less permeable matrix. It also explains the  
43 calibrated value of the ratio of mobile to total porosities used in previous modelling  
44 studies based on the dual-domain mass transfer approach. The results of this study  
45 underscore the importance of geologically plausible conceptualizations of the subsurface  
46 for making accurate predictions of the fate and transport of contaminants in highly  
47 heterogeneous aquifers. These conceptualizations may be developed through integration  
48 of raw geological data with expert knowledge, interpretation and appropriate geostatistical  
49 methods.

50

51 **Keywords.** solute transport, heterogeneity, MADE site, lithofacies

52

## 53 **1 Introduction and background**

54 Despite significant theoretical, experimental and computational advances, modelling  
55 of contaminant transport in heterogeneous aquifers is still challenging and subject of  
56 continuing debate in the scientific community [e.g., *Hadley and Newell*, 2014; *Neuman*,  
57 2014; *Molz*, 2015]. Yet, accurate simulations of the fate of contaminants are needed to  
58 address an ever growing demand for clean groundwater resources and an increasing  
59 interest in the use of the subsurface for the storage of nuclear waste, CO<sub>2</sub>, and heat.

60 Transport of nonreactive solutes through porous media is traditionally modelled with  
61 the advection–dispersion equation (ADE):

$$62 \frac{\partial C}{\partial t} = \nabla \cdot (\mathbf{D} \nabla C) - \nabla \cdot (\mathbf{v} C) \quad (1)$$

63 where  $C$  is concentration,  $\mathbf{v}$  is the macroscopic advective velocity, and  $\mathbf{D}$  is the  
64 hydrodynamic dispersion coefficient tensor. The latter is a function of the molecular  
65 diffusion coefficient,  $\mathbf{v}$ , and fixed longitudinal ( $\alpha_L$ ), horizontal transverse ( $\alpha_{TH}$ ) and  
66 vertical transverse ( $\alpha_{TV}$ ) dispersivities. Because the first term on the right hand side of  
67 Equation (1) is analogous to Fick’s law of molecular diffusion, solute transport described  
68 by the ADE is referred to as Fickian. However, tracer experiments at different scales very  
69 often show “anomalous” or non-Fickian features indicated by non-Gaussian asymmetric  
70 plumes, apparent loss of mass due to sequestration in relatively immobile zones, variations  
71 of mean transport velocity, and increases in the dispersion rates (i.e., dispersivity) with  
72 mean travel distance or in time [e.g., *Silliman et al.*, 1987; *Adams and Gelhar*, 1992;

73 *Haggerty et al.*, 2001; *Levy and Berkowitz*, 2003; *Cortis and Berkowitz*, 2004; *Bromly and*  
74 *Hinz*, 2004; *Bianchi et al.*, 2011a; *Cherubini et al.*, 2013].

75 For nonreactive tracers, non-Fickian transport is observed in aquifers characterized by  
76 sharp contrasts in hydraulic conductivity ( $K$ ) and by connectivity of high- $K$  regions  
77 [*Zheng and Gorelick*, 2003; *Klise et al.*, 2009; *Bianchi et al.*, 2011b; *Zhang et al.*, 2013],  
78 which are commonly found in alluvial aquifers [e.g., *Fogg*, 1986; *Webb and Anderson*,  
79 1996; *Fogg et al.*, 2000; *Labolle and Fogg*, 2001; *Baratelli et al.*, 2011; *Dell’Arciprete et*  
80 *al.*, 2014]. The inability of the Fickian approach to describe transport in such  
81 environments is explained by the fact that the travel distance required to reach asymptotic  
82 or scale-independent conditions for macroscopic Fickian dispersion is larger than the  
83 actual scale of the observed plumes [*Eggleston and Rojstacer*, 2000; *Berkowitz et al.*,  
84 2006; *Neuman and Tartakovsky*, 2009; *Srinivasan et al.*, 2010; *Molz*, 2015]. In fact, a  
85 scale-dependent (i.e., pre-asymptotic) behavior is observed for dispersivity, which is in  
86 contrast with the fixed macroscopic dispersivity derived from the central spatial moments  
87 of the plumes [e.g., *Adams and Gelhar*, 1992].

88 Field data collected at the research site in Columbus (Mississippi, USA), known as  
89 the Macrodispersion Experiment (MADE) site, have been used over the last three decades  
90 to investigate solute transport processes in alluvial aquifers. In particular, three large-scale  
91 natural gradient tracer experiments were conducted at this site in the mid ‘80s and in the  
92 ‘90s to test the applicability of the macrodispersion theory to explain solute transport in  
93 heterogeneous porous media [*Boggs et al.*, 1992; *Boggs et al.*, 1993; *Boggs et al.*, 1995]. A  
94 comprehensive list of references of the numerous studies concerning the geological and  
95 hydrogeological characterization of the MADE site, as well as the results, interpretation,  
96 and modelling of the tracer experiments, is given in the review paper by *Zheng et al.*  
97 [2011]. Although the physical heterogeneity of the aquifer was initially characterized by

98 more than 2500 flowmeter  $K$  measurements [Rehfeldt et al., 1992], the application of the  
99 macroscopic ADE failed to explain transport behavior observed during the three large-  
100 scale experiments [Adams and Gelhar, 1992; Eggleston and Rojstaczer 1998a, 1998b;  
101 Harvey and Gorelick, 2000; Feehley et al., 2000; Julian et al., 2001].

102 The failure of the macroscopic ADE to accurately describe the experimental data at  
103 the MADE site has been the motivation for the application of alternative modelling  
104 methods based on two approaches. The first approach is represented by non-Fickian  
105 transport models including the dual domain mass transfer model [Harvey and Gorelick,  
106 2000; Feehley et al., 2000; Guan et al., 2008; Llopis-Albert and Capilla, 2009], the  
107 fractional advective-dispersive equation [Benson et al. 2001; Zhang and Benson, 2008],  
108 and the continuous-time random walk [Berkowitz and Scher, 1998; Berkowitz et al., 2006].  
109 These models were able to provide a reasonable interpretation of the anomalous features  
110 of the observed plumes without an explicit representation of local-scale heterogeneity and  
111 connectivity, although their effect on transport is taken into account through mathematical  
112 formulations describing non-Fickian transport in time and space. A second approach,  
113 namely the local-ADE approach [e.g., Fiori et al., 2013], considers an explicit  
114 representation of small-scale heterogeneities based on the notion that if the velocity field  
115 is sufficiently characterized, then transport can be effectively described by Equation (1)  
116 considering advection, molecular diffusion, and local dispersion [e.g., Zheng and  
117 Gorelick, 2003; Salamon et al., 2007; Zheng et al., 2011; Fiori et al., 2013].

118 A recent application of the local-ADE approach at the MADE site is the study by  
119 Dogan et al. [2014], in which flowmeter measurements and additional high-resolution  $K$   
120 data, collected with the direct-push injection logger [DPIL; Liu et al., 2009; Bohling et al.,  
121 2012], were used to generate extremely detailed representations of the  $K$  field  
122 [Meerschaert et al., 2013] in a sector of the MADE site aquifer. This sector is about 1/6 of

123 the total extension of the domain investigated by the three large-scale tracer experiments.  
124 Transport simulations based on nine stochastic realizations of the  $K$  field showed a good  
125 agreement with experimental data collected during the first tracer test (MADE-1). Results  
126 from this work are significant because they provide strong confirmation that the local  
127 ADE approach can predict solute transport in very heterogeneous porous media such as  
128 the MADE site aquifer. However, the computational effort (on a grid of  $0.25\text{ m} \times 0.25\text{ m}$   
129  $\times 0.05\text{ m}$ , which amounts to approximately 111 million nodes for the entire MADE site  
130 domain of  $120\text{ m} \times 290\text{ m} \times 10\text{ m}$ ) and the amount of data used for generating the  $K$  field  
131 realizations (more than 5,500 measurements) were very substantial and not usually  
132 attainable.

133 Thus, in this work we test the hypothesis that we can explain the characteristics of the  
134 observed transport behavior at the MADE site with a much simpler local ADE-based  
135 model, without relying on exceedingly fine grid spacing or thousands of  $K$  data points.  
136 Differently from all the previous studies at the MADE site, we considered lithological data  
137 rather than  $K$  measurements (either from flowmeter or DPIL) to generate geologically  
138 consistent realizations of the spatial assemblage of five lithofacies, identified from a  
139 relatively small set of aquifer samples. These realizations were then used as basis for the  $K$   
140 fields in transport simulations of the MADE-2 experiment. The agreement between  
141 simulated and experimental data provides an unprecedented lithological explanation for  
142 the observed non-Fickian transport behavior at the MADE site, while also demonstrating  
143 that this behavior can be adequately simulated by a local ADE-based model without an  
144 extraordinarily high-resolution characterization of the  $K$  field.

145

146

147 **2 Data**

148 Lithological data consist of 411 aquifer samples collected from 38 boreholes covering  
149 the total thickness of the aquifer (about 11 m on average). Location of these boreholes is  
150 shown in Figure 1, while lithological descriptions and the results of grain-size analyses  
151 performed on a subset of 214 soil samples from 29 boreholes are presented in a  
152 preliminary hydrogeological characterization study of the MADE site [Boggs *et al.*, 1990].  
153 Aquifer sampling was conducted using a hollow stem auger and split core barrel samplers  
154 [Boggs *et al.*, 1990; 1992] and samples were generally collected at 1.5 meter intervals.  
155 The majority of the boreholes are located in the southern sector of the site, with only 6  
156 boreholes located within the boundary of the network of multilevel sampling wells used to  
157 monitor concentrations during the tracer experiments.

158 Grain size data consist of percentages of gravel (diameter of soil grains greater than  
159 4.76 mm), sand (diameter between 0.074 mm and 4.76 mm) and fines (diameter smaller  
160 than 0.074 mm). Values of the 10<sup>th</sup> ( $d_{10}$ ), 25<sup>th</sup> ( $d_{25}$ ), and 60<sup>th</sup> ( $d_{60}$ ) percentiles of the  
161 cumulative grain size distribution are also available. Most of the aquifer at the MADE site  
162 consists of bimodal mixtures of gravel and sand with a low percentage of fines (less than  
163 5% on average). In general, mixtures of gravel, sand and fines are more predominant in  
164 the most superficial part of the aquifer (up to 4 m of depth). Gravel content decreases with  
165 depth (less than 25% on average), and it is particularly low toward the bottom boundary of  
166 the aquifer represented by low-permeable marine deposits of the Eutaw formation. This  
167 deeper portion of the aquifer consists mostly of well sorted sand with fines content  
168 ranging from 1% up to 22%. Additional details on the vertical variability of gravel, sand,  
169 and fines content are provided by Boggs *et al.* [1990, 1992].

170

### 171 3 Methods

#### 172 3.1 Lithofacies identification

173 Aquifer samples were classified into five lithofacies on the basis of the relative  
174 content of gravel (G), sand (S) and fines (f), as well as of values of  $d_{10}$ ,  $d_{25}$  and of the  
175 uniformity coefficient ( $U = d_{60} / d_{10}$ ). The criteria used for the identification of these  
176 lithofacies and key parameters are summarized in Table 1.

177 Lithofacies HCG (“highly conductive gravel”) and GS (“gravel with sand”), which  
178 represent the 12% and the 18% of the samples respectively, consist of poorly sorted sandy  
179 gravels (gravel content > 50%) with minor fines (< 5%). The two lithofacies are  
180 distinguishable on the basis of the  $d_{10}$  (> 0.25 mm for HCG) and  $d_{25}$  values (> 1.0 mm for  
181 HCG). The two threshold values of 0.25 mm and 1.0 mm were chosen to be corresponding  
182 to the smallest grain sizes to define “medium sands” and “very coarse sands” according to  
183 the widely used soil classification by *Krumbein* [1934]. Grain size in HCG is also  
184 relatively more uniform than in GS ( $U = 30$  vs. 41). In particular, HCG represents coarse  
185 gravelly sediments, as shown by the values of the  $d_{60}$  with values ranging between 6.4 mm  
186 and 19.7 mm. Lithofacies SGf (“sand, gravel and fines”) consists of mixtures of gravel,  
187 sand and fines in various proportions. In general, sand content is higher than that of  
188 gravel, although some samples have gravel content up to 70%. The content of fines is  
189 higher than 5% in all samples. This lithofacies is the most represented in the aquifer  
190 samples (35%). Lithofacies SG (“sand and gravel”) consists of moderately sorted gravelly  
191 sands and represents the 14% of the samples. On average, SG has moderately high sand  
192 content (about 65%), minimal fines (< 3% average), and  $d_{10}$  values similar to those in GS,  
193 albeit with more uniformity in the grain-size distribution ( $U=16$ ). Lithofacies S (“sand”)  
194 consists of well sorted sand (sand content > 85%; average  $U = 2.6$ ) with an average  $d_{10}$   
195 values similar to that in SGf (0.14 mm and 0.12 mm, respectively).

196

### 197 3.2 Stochastic simulation of lithofacies assemblage

198 Spatial continuity of the identified lithofacies was initially assessed along cross-  
199 sections intercepting the boreholes to identify transition trends and estimate lateral and  
200 vertical extensions. In a second stage, transition probabilities between lithofacies were  
201 calculated and modelled with a three-dimensional Markov chain in a conditional  
202 simulation framework [Carle, 1999]. The transition probability approach introduced by  
203 Carle and Fogg [1996, 1997] has been used to produce geologically consistent  
204 representations of subsurface heterogeneity by preserving the connectivity of lithofacies  
205 and juxtapositional tendencies [e.g., Carle et al., 1998; Weissmann and Fogg, 1999; Ritzi,  
206 2000; Ritzi et al., 2004; Lee et al., 2007; Dai et al., 2007; Ye and Khaleel, 2008; Bianchi et  
207 al., 2011b]. Differently from traditional variogram-based geostatistical methods, with this  
208 approach the spatial structure of the data is represented by transition probabilities, which  
209 are defined in terms of the following conditional probability:

$$210 \quad t_{i,k}(\mathbf{h}) = \Pr \{k(\mathbf{x} + \mathbf{h}) | i(\mathbf{x})\} \quad (2)$$

211 where  $t_{i,k}$  is the transition probability from lithofacies  $i$  to lithofacies  $k$ , and  $\mathbf{x}$  and  $\mathbf{h}$  are the  
212 spatial location and lag distance vectors. Because, from Equation (2), the occurrence of  
213 lithofacies  $k$  at location  $\mathbf{x} + \mathbf{h}$  is only dependent on the occurrence of lithofacies  $i$  at  
214 location  $\mathbf{x}$ , three-dimensional continuous-lag Markov Chain models can be developed to  
215 model discrete transition probabilities observed in the data. In this work, the fitting of a  
216 3D Markov chain to the transition probabilities measured in the borehole data was  
217 performed by adjusting embedded transition probabilities and mean length and thickness  
218 values of lithofacies (Figure 2). Because of the relatively small number of boreholes, the  
219 estimation of mean length values from the plots of auto-transition probabilities in the  
220 horizontal direction is characterized by a certain degree of uncertainty. Therefore, in order

221 to apply a more objective criterion for the estimation of the spatial correlation of the  
222 lithofacies in the horizontal direction, we have chosen to apply an early lag data approach  
223 [Carle and Fogg, 1997] in which the lag-one transition probability was used to compute  
224 the Markov chain model. This fit also produces probabilistic estimates of the mean length  
225 for each lithofacies (Figure 2a). We also tested the sensitivity of the transport modelling  
226 results with respect to this choice, especially regarding variations of the mean length of  
227 lithofacies HCG. The results of this sensitivity analysis will be discussed later. The  
228 calibrated Markov chain model also assumes isotropic behavior in the horizontal plane  
229 and lithofacies SGf as the background category. Volumetric proportions of the lithofacies,  
230 represented by the sill of the transiograms in the model, are also assumed equal to the  
231 proportions exhibited by the borehole data. Modeled transition probabilities and values of  
232 mean length and thickness for each lithofacies (Table 1) are reasonable and consistent  
233 with the spatial continuity assessed in the cross-sections. The mean lengths of the  
234 lithofacies inferred from the transition probability analysis is of the order of tens of  
235 meters, while thicknesses are in the order of a meter indicating higher variability along the  
236 vertical direction as in shown by previous investigations [e.g., Rehfeldt *et al.*, 1992;  
237 Bohling *et al.*, 2012]

238

### 239 3.3 Flow and transport simulations

240 A three-dimensional stochastic flow and transport model was implemented to  
241 simulate the second large scale tracer experiment (MADE-2; Boggs *et al.*, 1993). The  
242 block-centered numerical grid, with a total size of 120 m × 290 m × 10 m (Figure 1), has a  
243 resolution of 2 m in the horizontal plane and 0.5 m in the vertical direction. The total  
244 number of cells of the numerical grid is about  $1.82 \times 10^4$ , which is about 18 times less than

245 the number of cells in the model by *Dogan et al.* [2014], even though the latter considers a  
246 smaller domain.

247 The  $K$  fields in the numerical simulations are directly linked to the spatial  
248 distribution of the identified lithofacies. These were generated according to the following  
249 procedure. In a first step,  $K$  values for each sample were estimated with the Kozeny-  
250 Carman empirical formula [e.g., *Riva et al.*, 2010]:

$$251 \quad K = 8.3 \times 10^{-3} \frac{g\theta^3}{\nu(1-\theta)^2} d_e^2 \quad (3)$$

252 where  $g$  is gravity (9.81 m<sup>2</sup>/s),  $\nu$  is the kinematic coefficient of viscosity of water (1.002  
253 m<sup>2</sup>/s at 20 °C),  $d_e$  is a representative grain diameter, and  $\theta$  is porosity. Porosity was  
254 estimated according to the empirical formula of *Vucovic and Soro* (1992) :

$$255 \quad \theta = 0.255(1 + 0.83^U) \quad (4)$$

256 Porosity values for each lithofacies (Table 1) and the average of all the samples (0.307)  
257 are similar to measurements in collected aquifer samples (*Boggs et al.*, 1990; *Boggs et al.*,  
258 1992). Although there are different interpretations for  $d_e$  in the literature [e.g., *Koltermann*  
259 *and Gorelick*, 1995], here it was assumed to be corresponding to  $d_{10}$  for lithofacies GS,  
260 SG, SGf and S. There is in fact experimental evidence showing the reliability of this  
261 assumption in medium to coarse gravelly sands [*Odong*, 2007] and in well to moderately  
262 sorted sand/gravel mixtures [e.g., *Barahona-Palomo et al.*, 2011]. The average between  
263  $d_{10}$  and  $d_{25}$  was chosen instead for lithofacies HCG because of lower sand content and  
264 significantly coarser grain size (Table 1). With this choice, estimated  $K$  values for the  
265 HCG samples are also more comparable with previous  $K$  estimates [*Boggs et al.*, 1990;  
266 *Eggleston and Rojstaczer*, 1998b] based on a different empirical formula, which was  
267 developed specifically for gravel and sand mixtures [*Seiler*, 1973]. In the subsequent  
268 discussion, we will test the effect of this assumption on simulated transport behavior. In a

269 second step, descriptive statistics of the log transformed  $K$  estimates were computed for  
270 the five lithofacies (Table 1). As expected given the coarsest grain size, statistical analysis  
271 of the estimated  $K$  values for each lithofacies (Figure 3) indicates that HCG is  
272 significantly the most conductive lithofacies, with a mean  $K$  value that is about 1.5 to 2  
273 orders of magnitude higher than the mean values of the other lithofacies. Next, three-  
274 dimensional conditional realizations of the spatial assemblage of lithofacies were  
275 generated according to the calculated transition probabilities and fitted Markov chain  
276 model [Carle *et al.*, 1998; Carle, 1999]. In the transport model domain the realizations are  
277 conditioned to the lithofacies identified in the samples from 6 boreholes (Figure 1). In the  
278 final step, an appropriate  $K$  value was assigned to each cell of the numerical grid of  
279 transport simulations according to the simulated distribution of lithofacies. This value was  
280 randomly generated from the truncated lognormal distribution, with mean and standard  
281 deviation equal to the corresponding values for each lithofacies. One standard deviation  
282 below and above the mean were considered as truncation thresholds to avoid excessive  
283 overlapping among different lithofacies and preserve the lithological structure on the  
284 generated  $K$  fields.

285 Groundwater flow was simulated in three stress periods of the duration of 2, 158 and  
286 168 days using MODFLOW-2005 [Harbaugh, 2005]. The duration of the first stress  
287 period was chosen to represent the tritium injection. During the MADE-2 experiment, a  
288 total of  $9.3 \text{ m}^3$  of a solution containing tritium was injected for approximately 48 hours  
289 through a linear array of five injection wells, spaced 1 m apart, and centered on the origin  
290 of the Cartesian coordinates system in Figure 1 (Boggs *et al.* 1993). The injection wells  
291 were screened at a depth interval between 57.5 m and 58.1 m a.s.l. The injection procedure  
292 in the model was simplified such that only two cells of the numerical grid were considered  
293 for the injection. However, the location of these cells and the total injected tritium mass

294 (0.5387 Ci) are consistent with the experimental conditions. The remaining stress periods  
295 were chosen to represent two distinct climatic periods observed over the 328 days of the  
296 experiment, which are clearly shown by significant water table fluctuations registered by  
297 the groundwater level monitoring network [Boggs *et al.*, 1993; Stauffer *et al.*, 1994; Guan  
298 *et al.*, 2008]. Accordingly, average values of groundwater levels measured at different  
299 wells during these two climatic periods were used to define specified-head boundary  
300 conditions at  $Y = -20$  m and  $Y = 270$  m, while no-flow boundary conditions were  
301 imposed at  $X = -50$  m,  $X = 70$  m and  $Z = 52$  m. Despite the possible importance of  
302 transient flow conditions on transport at the MADE site [Llopis-Albert and Capilla, 2009],  
303 flow was assumed steady state in all stress periods. The ratio between vertical and  
304 horizontal  $K$  assumed in the model (0.13) is based on the results of a pumping test  
305 conducted at the MADE site [Boggs *et al.*, 1990].

306 Transport simulations based on Equation (1) were performed with MT3DMS  
307 [Zheng, 2010] with the advection component solved with the total-variation-diminishing  
308 (TVD) scheme to minimize numerical dispersion given the relative coarseness of the grid  
309 and avoid mass balance inconsistencies. A Courant number of 0.75 was used for all  
310 transport simulations. Porosity values were assigned to the grid according to the  
311 lithofacies distribution. These correspond to the average of the values estimated with  
312 Equation 4 for each lithofacies (Table 1). Other input parameters include a molecular  
313 diffusion coefficient for tritium of  $1.16 \times 10^{-9}$  m<sup>2</sup>/s [Salomon *et al.*, 2007],  $\alpha_L$  equal to 1 m  
314 [Feehley *et al.*, 2000; Llopis-Albert and Capilla, 2009], and values of  $\alpha_{TH}$  and  $\alpha_V$  of one  
315 and two orders of magnitude lower than  $\alpha_L$ .

316 The accuracy of the implemented model was tested by comparing simulated and  
317 observed 1-D longitudinal mass distributions at 27, 132, 224, and 328 days after the

318 injection. These times correspond to the first four “snapshots” of the MADE-2 experiment  
 319 [*Boggs et al.*, 1993]. For the calculation of experimental mass distributions, the mass  
 320 along each monitoring well was integrated vertically and then interpolated in 2-D over the  
 321 same grid used for flow and transport simulations. Observed and simulated mass  
 322 distributions for each snapshot were then obtained by integrating the fraction of total  
 323 recovered mass in 30 equally spaced zones of 10 m width along the general flow direction  
 324 ( $y$  axis).

325 The mean longitudinal displacement ( $\bar{y}$ ) and the longitudinal variance of the  
 326 observed and simulated 1-D mass profiles ( $\sigma_{yy}^2$ ) were also calculated on the basis of the  
 327 central spatial moments according to the following equations (e.g., *Adams and Gelhar*,  
 328 1992):

$$329 \quad \bar{y} = M_1 / M_0 \quad (5)$$

330 and

$$331 \quad \sigma_{yy}^2 = M_2 / M_0 - M_1^2 / M_0 \quad (6)$$

332 The generic spatial moment  $M_i$  for the observed and simulated longitudinal mass profiles  
 333 was calculated with the following equation:

$$334 \quad M_i = \sum_{p=1}^N m_p y^i \quad (7)$$

335 where  $m_p$  is the fraction of recovered mass at the point  $p$  of coordinates  $y$ , and  $N$  is the total  
 336 number of points. Note that since tritium mass was normalized with the total recovered  
 337 mass, the zero-th moment  $M_0$  is equal to 1 for both observed and simulated mass profiles.

338

#### 339 4 Results and discussion

340 The ensemble mean and median of 1-D longitudinal mass distributions from 500  
341 Monte Carlo realizations of the model are shown in Figure 4a-d. The interquartile range is  
342 also reported to provide a description of the variability of the simulated results. In general,  
343 the model is accurate in reproducing the mass accumulation near the injection site and the  
344 spreading to the far field. The model tends to overestimate the position of the edge of the  
345 plume in the first two snapshots, even though the mismatch is limited to fractions of  
346 recovered mass below 0.01. At later times (224 and 328 days), the model does not match  
347 the relative peak of mass observed between 160 m and 200 m from the injection site. This  
348 peak is most probably the effect of transient variations in the flow field during the  
349 experiment as suggested by fluctuations in the water table of up to 30% of the saturated  
350 thickness, which were observed during later stages of the MADE-2 test [Stauffer *et al.*,  
351 1994; Llopis-Albert and Capilla, 2009]. These variations were not considered in the  
352 presented model. A better match between observed and simulated mass profiles could also  
353 be probably achieved with calibration of some of the model input parameters (e.g.,  
354 porosity and  $K$  values of the lithofacies, boundary conditions). However, a calibration  
355 procedure not only is beyond the scope of the present work, but also would reduce the  
356 predictability of our lithofacies approach and compromise the insight about its  
357 transferability to other sites. Notwithstanding these simplifications, the implemented  
358 transport model is able to capture the overall characteristics of the MADE-2 plume with  
359 reasonable accuracy, especially considering the limited number of hard conditioning  
360 points used in the stochastic realizations of subsurface heterogeneity.

361 Reasonable accuracy is further confirmed by comparisons between observed and  
362 simulated central moments (Figure 5a-c). The percentage error between the observed  
363 longitudinal displacement and the ensemble mean of the simulated values is between 11%

364 and 51%. The highest discrepancy is calculated for the displacement at 132 days, because  
365 simulated plumes tend to advance too rapidly (9.2 m vs. 13.9 m). The error between  
366 observed and simulated displacement at 224 and 328 is around 25%, but this discrepancy  
367 is strongly influenced by the relative peak of mass observed at later times and by the  
368 extremely rapid movement of the center of mass observed between 132 and 224 days. One  
369 important aspect regarding the proposed model shown in Figures 5b and 5c is that the  
370 second central moment representing the longitudinal variance of the plume grows at  
371 different rates in both time and space. This characteristic and the asymmetric shape of the  
372 simulated mass distributions are indicative of non-Fickian transport behavior.

373 From the comparison between the spatial distributions of the identified lithofacies  
374 (Figure 6a), the corresponding  $K$  fields (Figure 6b), and the location of the plume front at  
375 different times (Figure 6c), it is evident that the asymmetric shape of the plume and the  
376 rapid movement of the edge are controlled by the location and the lateral continuity of the  
377 highly conductive lithofacies HCG. Given the dimension of the simulated domain in the  
378 longitudinal direction (145 cells) and its mean length (30 m = 15 cells), the percolation  
379 threshold for lithofacies HCG is expected to be around 0.14, according to *Harter* [2005].  
380 Because the percolation threshold corresponds to the critical volumetric fraction for which  
381 there is occurrence of one cluster of cells spanning the entire domain, the estimated  
382 volumetric fraction of 0.12 for lithofacies HCG indicates that this lithofacies defines an  
383 interconnected network of high- $K$  values that almost fully percolate the MADE site  
384 aquifer. This result provides a further confirmation of the hypothesis advanced by several  
385 previous studies [e.g., *Fogg*, 1986; *Fogg et al.*, 2000; *Labolle and Fogg*, 2001; *Zheng and*  
386 *Gorelick*, 2003; *Zheng et al.*, 2011; *Moltz*, 2015] that the “anomalous” transport behavior  
387 observed in heterogeneous alluvial aquifers is mostly the effect of connectivity of high- $K$   
388 sediments. This connectivity enhances fast advective transport of a fraction of mass along

389 preferential flow-paths, while a larger fraction travels in a relatively less permeable  
390 matrix. In the matrix, the role of diffusive transport is more significant especially in  
391 directions perpendicular to the main flow. When high- $K$  zones connectivity is taken into  
392 account, faster than expected breakthrough times and late-time tailing of contaminants  
393 concentrations, which are commonly observed in contaminated aquifer sites, can be  
394 successfully predicted [*Labolle and Fogg, 2001*].

395 The influence of lithofacies HCG on the velocity field and consequently on advective  
396 transport is also shown by the analysis of the frequency distributions of the generated  $K$   
397 fields (Figure 7). These are clearly bimodal, with the majority of the  $\log_{10}(K)$  values  
398 clustered around a value of about 0.75 m/d, and a smaller set of values around the average  
399 value for lithofacies HCG (Table 1). Comparisons between the distribution for the  
400 generated  $K$  fields and the distributions of  $K$  data previously collected at the MADE site  
401 with two different methods [*Rehfeldt et al., 1992; Bohling et al., 2012*] indicate similarity  
402 between the modal value of the  $K$  estimates for lithofacies GS, SGf, SG and S and average  
403 value of the flowmeter measurements. The  $K$  estimates for lithofacies HCG are also  
404 comparable to the upper tails of the distributions of both the flowmeter and the DPIL data.  
405 However, the three  $K$  data sets differ in terms of sample variances, and the correlation  
406 between corresponding values at different depths in boreholes located within a 3.5 m  
407 radius is generally poor. A discussion of the possible causes for the mismatch between the  
408 flowmeter data and the DPIL data is presented by *Bohling et al.* [2012], while mismatches  
409 between the  $K$  estimates based on grain-size analysis and flowmeter data have been also  
410 observed in other alluvial aquifers [*Barahona-Palomo et al., 2011; Gutting et al., 2015*].  
411 As for these other aquifers, the lack of correlation between types of  $K$  data for the MADE  
412 site aquifer is most likely explained by the difference in the support scale associated with

413 each method, which ranges from a few centimeters for DPIL, to about 1.5 decimeters for  
414 the flowmeter measurements, up to several decimeters for the grain-size estimates.

415 Our interpretation may also provide a geological explanation for the success of the  
416 dual-domain mass transfer rate approach (DDM) in reproducing the experimental data at  
417 this site [Harvey and Gorelick, 2000; Feehley et al., 2000; Guan et al., 2008; Bianchi et  
418 al., 2011a]. This approach simulates transport in two distinct but overlapping mobile and  
419 immobile domains, each characterized by a certain porosity value, and the total porosity of  
420 the system is given by the sum of the mobile and immobile porosities. A mass transfer rate  
421 coefficient controls the exchange of solute mass between the two domains. According to  
422 the dual-domain conceptualization, pore space in the mobile domain is filled with water  
423 that can actually move through the porous structure and solute transport is mainly due to  
424 advection. On the other hand, pores in the immobile domain are filled with stagnant water  
425 and molecular diffusion is the main transport process. This separation into two mobile and  
426 immobile domains is therefore particularly suitable for reproducing transport when  
427 interconnected high- $K$  sediments (i.e., the mobile domain) are embedded in a relatively  
428 lower permeable matrix (i.e., the immobile domain).

429 Because our results suggest that the lithofacies HCG can be considered the mobile  
430 domain through which fast advective transport occurs, it is very noteworthy that the  
431 volumetric fraction estimated from the borehole data (0.12) corresponds to the calibrated  
432 value of the ratio between mobile and total porosities ( $1/8 = 0.125$ ) of dual-domain  
433 models, which were able to fit the observed plume spreading at the MADE site [Zheng et  
434 al., 2011 and references therein]. As a confirmation, we implemented a DDM model  
435 (single-rate) based on a homogenous field with  $K$  equal to the ensemble mean of the  
436 equivalent  $K$  values for a subset of realizations of the  $K$  field. For each realization, the  
437 equivalent  $K$  was estimated by applying Darcy's law between the two specified-head

438 boundaries of the simulated domain in Figure 1, and by assuming a preservation of the  
439 total discharge. This approach is similar to that used by *Liu et al.* [2007] to test the  
440 applicability of the DDM to represent transport in binary  $K$  fields characterized by  
441 decimeter-scale highly conductive channels. The model also assumes a mobile to total  
442 porosity ratio equal to the volumetric fraction of HCG. Comparisons between observed  
443 and simulated plumes show that we can match the observed the transport behavior with  
444 adequate accuracy by a simple calibration of the mass transfer rate coefficient (Figure 8  
445 and Figure 5d). As in the model proposed by *Guan et al.* [2008], calibrated values for this  
446 parameter indicate that the single-rate mass transfer coefficient is scale-dependent and  
447 decreases with time.

448 Results shown in Figure 4a-d are based on the input parameters of Table 1. Because  
449 of the uncertainty associated with some of these parameters and the dominant influence of  
450 lithofacies HCG on the simulated transport behavior, we also analyzed the sensitivity of  
451 the results with respect to changes of  $K$  and mean length for this lithofacies. The results  
452 for the snapshot at 328 days are shown in Figure 4e. When lithofacies HCG is ignored in  
453 the generation of the  $K$  fields and its  $K$  value is assumed equal to that of lithofacies GS,  
454 the mass distribution showed very limited spreading and a symmetric shape. A similar  
455 result was obtained in a scenario in which the  $K$  of lithofacies HCG is estimated by  
456 considering the  $d_{10}$  as the value for  $d_e$  in Equation 2. The model is also sensitive with  
457 respect to changes of the mean length of lithofacies HCG. However, even when the mean  
458 length is assumed to be one half of the value in Table 1, we still observe a significantly  
459 asymmetric mass distribution although the leading edge of the plume is about 40 m  
460 shorter. This result indicates that even if a small range of mean length values would fit the  
461 estimated auto-transition probabilities equally well for lithofacies HCG (Figure 2a), the  
462 main conclusion regarding its role on controlling non-Fickian transport is still valid.

463

## 464 **5 Conclusions**

465 Site-scale transport behavior observed during one of the MADE site experiments  
466 (MADE-2) was effectively reproduced with a relatively simple, local ADE-based model.  
467 The physical aquifer heterogeneity in the transport model was conceptualized and  
468 represented by 3-D realizations of the spatial distribution of lithofacies identified from  
469 aquifer samples collected from 39 boreholes, mostly located outside the domain used for  
470 transport simulations. The lithofacies approach appears to have provided an unprecedented  
471 explanation to “anomalous” plume-scale behavior at the MADE site that has motivated a  
472 long line of studies over the past 30 years. Furthermore, results suggest that such behavior  
473 can be reproduced with a model based on a much smaller set of aquifer property data than  
474 previously thought possible.

475 In particular, this analysis shows that some of the non-Fickian features of the  
476 observed plume can be explained by a highly permeable lithofacies with limited (less than  
477 1 m) vertical extent and moderate (>10 m) horizontal correlation. The presence of a  
478 network of well interconnected highly permeable sediments embedded in a less permeable  
479 matrix has been previously suggested for the MADE site [*Harvey and Gorelick, 2000*;  
480 *Zheng and Gorelick, 2003*] and tested in small sectors of the investigated domain [*Liu et*  
481 *al., 2010*; *Ronayne et al., 2011*; *Bianchi et al., 2011a, 2011b*], but never assessed at the  
482 scale of the large scale tracer experiments. In the context of about three decades of  
483 research work at the MADE site, the identification of the most conductive lithofacies  
484 (HCG) from borehole lithological data is a significant result providing a previously  
485 elusive, simple explanation for the observed non-Fickian transport behavior from a  
486 geological perspective.

487 The proposed model of physical heterogeneity for the MADE site aquifer seems also  
488 to provide a lithological basis for the success of dual-domain mass transfer rate approach  
489 in reproducing non-Fickian transport behavior at this site [Zheng *et al.*, 2011]. In this  
490 respect, this work can also be seen as a first successful attempt to infer the ratio between  
491 mobile to total porosities, which is at the basis of dual-domain conceptualization, from  
492 grain-size analysis data and volumetric fractions of lithofacies.

493 Even though this study is focused on a particular alluvial aquifer, the impact of the  
494 results is broader because they show that if the geological structure – here represented by  
495 the spatial distribution of the lithofacies – is properly represented in the 3-D hydraulic  
496 conductivity field, then solute transport in heterogeneous aquifers can be accurately  
497 simulated with local ADE-based models without relying on exceedingly fine grid spacing  
498 or high-resolution  $K$  data. The incorporation of the geological structure in the physical  
499 model of heterogeneity also provides verifiable explanations for the observed plume  
500 behavior. Therefore, this work underscores the importance of geologically based  
501 representations of the subsurface, which can be developed through integration of raw  
502 geological data (e.g., borehole logs, aquifer analog descriptions, geophysical surveys) with  
503 expert knowledge, interpretation and appropriate geostatistical methods.

504

505 **Acknowledgments.** This work was undertaken as part of the “Research Fellowship  
506 Programme” funded by the British Geological Survey (Natural Environment Research  
507 Council). Additional support was provided by the National Natural Science Foundation of  
508 China (Grant No. 41330632). We are grateful to Graham Fogg, Daniel Feinstein, and  
509 Erica Siirila-Woodburn for their constructive review comments , which have improved the  
510 final manuscript. Co-author Bianchi publishes with the permission of the Executive  
511 Director of the British Geological Survey. Lithological data used in this study can be

512 found in the referenced report *Boggs et al.* [1990]. Tracer data used in this study are  
513 available in the referenced report *Boggs et al.* [1993].

514

## 515 **References**

- 516 Adams, E.E., and L.W. Gelhar (1992), Field study of dispersion in a heterogeneous  
517 aquifer: 2. Spatial moments analysis, *Water Resour. Res.*, 28(12), 3293–3307,  
518 doi:10.1029/92WR01757.
- 519 Barahona-Palomo, M., M. Riva, X. Sanchez-Vila, E. Vazquez-Sune, and A. Guadagnini  
520 (2011), Quantitative comparison of impeller flowmeter and particle-size distribution  
521 techniques for the characterization of hydraulic conductivity variability, *Hydrogeol. J.*,  
522 19(3), 603–612, doi:10.1007/s10040-011-0706-5.
- 523 Baratelli, F., M. Giudici, and C. Vassena, C. (2011), Single and dual domain models to  
524 evaluate the effects of preferential flow paths in alluvial porous sediments, *Transp.*  
525 *Porous Med.*, 87, 465–484, doi:10.1007/s11242-010-9695-4.
- 526 Barlebo, H. C., M. C. Hill, and D. Rosbjerg (2004), Investigating the Macrodispersion  
527 Experiment (MADE) site in Columbus, Mississippi, using a three-dimensional inverse  
528 flow and transport model, *Water Resour. Res.*, 40, W04211,  
529 doi:10.1029/2002WR001935.
- 530 Benson, D. A., R. Schumer, M. M. Meerschaert, and S. W. Wheatcraft (2001), Fractional  
531 dispersion, Lévy motion, and the MADE tracer tests, *Transport in Porous Media*, 42,  
532 211–240, doi: 10.1023/A:1006733002131.
- 533 Berkowitz, B., A. Cortis, M. Dentz, and H. Scher (2006), Modeling non-fickian transport  
534 in geological formations as a continuous time random walk, *Rev. Geophys.*, 44,  
535 RG2003, doi:10.1029/2005RG000178.
- 536 Bianchi, M., C. Zheng, G.R. Tick, and S.M. Gorelick (2011a), Investigation of Small-  
537 Scale Preferential Flow with a Forced-Gradient Tracer Test, *Groundwater*, 49, 503–  
538 514, doi: 10.1111/j.1745-6584.2010.00746.
- 539 Bianchi, M., C. Zheng, C. Wilson, G. R. Tick, G. Liu, and S. M. Gorelick (2011b), Spatial  
540 connectivity in a highly heterogeneous aquifer: From cores to preferential flow paths,  
541 *Water Resour. Res.*, 47, W05524, doi:10.1029/2009WR008966.
- 542 Bohling, G.C., G. Liu, S.J. Knobbe, E.C. Reboulet, D.W. Hyndman, P. Dietrich, and J.J.  
543 Butler Jr. (2012), Geostatistical analysis of centimeterscale hydraulic conductivity

544 variations at the MADE site, *Water Resour. Res.*, 48, W02525,  
545 doi:10.1029/2011WR010791.

546 Boggs, J. M., S. C. Young, D. J. Benton, and Y. C. Chung (1990). Hydrogeologic  
547 characterization of the MADE site, Interim Rep. EN-6915, Electr. Power Res. Inst.,  
548 Palo Alto, Calif.

549 Boggs, J.M., S.C. Young, and L.M. Beard (1992), Field study of dispersion in a  
550 heterogeneous aquifer 1. Overview and site description, *Water Resour. Res.*, 28(12),  
551 3281–3291.

552 Boggs, J.M., L.M. Beard, S.E. Long, M.P. McGee, W.G. MacIntyre, C.P. Antworth, and  
553 T.B. Stauffer (1993), Database for the Second Macrodispersion Experiment (MADE-  
554 2), Tech. Rep. TR-102072, Electric Power Res. Inst., Palo Alto, California.

555 Boggs, J.M., J.A. Schroeder, and S.C. Young (1995), Data to support model development  
556 for natural attenuation study. Report No. WR28-2-520-197. TVA Engineering  
557 Laboratory, Tennessee Valley Authority, Norris, Tennessee

558 Bromly, M., and C. Hinz (2004), Non-Fickian transport in homogeneous unsaturated  
559 repacked sand, *Water Resour. Res.*, 40, W07402, doi:10.1029/2003WR002579.

560 Carle, S.F. (1999), T-PROGS: Transition Probability Geostatistical Software, version 2.1.  
561 Davis, California: University of California.

562 Carle, S.F., and G.E. Fogg (1996), Transition probability-based indicator geostatistics,  
563 *Math. Geol.*, 28(4), 453–476.

564 Carle S.F., and G.E. Fogg (1997), Modeling spatial variability with one and  
565 multidimensional continuous-lag Markov chains, *Math. Geol.*, 29(7), 891–918.

566 Carle S.F., E.M. LaBolle, G.S. Weissmann, D. VanBrocklin, and G.E. Fogg (1998),  
567 Geostatistical simulation of hydrostratigraphic architecture: a transition probability /  
568 Markov approach, in *Concepts in Hydrogeology and Environmental Geology No. 2*,  
569 *SEPM Special Publication*, p. 147–170

570 Cherubini, C., C.I. Giasi, and N. Pastore (2013), Evidence of non-Darcy flow and non-  
571 Fickian transport in fractured media at laboratory scale, *Hydrol. Earth Syst. Sci.*, 17,  
572 2599-2611, doi:10.5194/hess-17-2599-2013.

573 Cortis, A., and B. Berkowitz (2004), Anomalous transport in “classical” soil and sand  
574 columns, *Soil Science Society of America Journal*, 68, no. 5, 1539-1548.

575 Dai, Z., A. Wolfsberg, Z. Lu, and R. Ritzi Jr. (2007), Representing aquifer architecture in  
576 macrodispersivity models with an analytical solution of the transition probability  
577 matrix, *Geophys. Res. Lett.*, 34, L20406, doi:10.1029/2007GL031608.

578 Dell'Arciprete, D., C. Vassena, F. Baratelli, M. Giudici, R. Bersezio, and F. Felletti  
579 (2014), Connectivity and single/dual domain transport models: tests on a point-  
580 bar/channel aquifer analogue, *Hydrogeology Journal*, 22(4), 761-778.  
581 doi:10.1007/s10040-014-1105-5 .

582 Dogan, M., R. L. Van Dam, G. Liu, M. M. Meerschaert, J. J. Butler Jr., G. C. Bohling, D.  
583 A. Benson, and D. W. Hyndman (2014), Predicting flow and transport in highly  
584 heterogeneous alluvial aquifers, *Geophys. Res. Lett.*, 41, 7560–7565,  
585 doi:10.1002/2014GL061800.

586 Eggleston, J. R., and S. Rojstaczer (1998a), Identification of large-scale hydraulic  
587 conductivity trends and the influence of trends on contaminant transport, *Water Resour.*  
588 *Res.*, 34(9), 2155–2168, doi:10.1029/98WR01475.

589 Eggleston, J. R., and S. Rojstaczer (1998b), Inferring spatial correlation of hydraulic  
590 conductivity from sediment cores and outcrops, *Geophys. Res. Lett.*, 25, 2317–2320,  
591 1998.

592 Eggleston, J.R., and S.A. Rojstaczer (2000), Can we predict subsurface mass transport?  
593 *Environmental Science and Technology* 34, 18, 4010–4017, doi:10.1021/es000903s.

594 Feehley C.E., C. Zheng, and F.J. Molz (2000), A dual-domain mass transfer approach for  
595 modeling solute transport in heterogeneous porous media, application to the MADE  
596 site, *Water Resour. Res.*, 36(9), 2501–2515, doi:10.1029/2000WR900148.

597 Fiori, A., G. Dagan, I. Jankovic, and A. Zarlenga (2013), The plume spreading in the  
598 MADE transport experiment: Could it be predicted by stochastic models? *Water*  
599 *Resour. Res.*, 49, 2497–2507, doi:10.1002/wrcr.20128.

600 Fogg, G. E. (1986), Groundwater Flow and Sand Body Interconnectedness in a Thick,  
601 Multiple-Aquifer System, *Water Resour. Res.*, 22(5), 679–694,  
602 doi:10.1029/WR022i005p00679.

603 Fogg, G.E., S.F. Carle, and C. Green (2000), Connected-network paradigm for the alluvial  
604 aquifer system. In: Zhang, D., C.L. Winter, eds., Theory, modeling, and field  
605 investigation in hydrogeology: A special volume in honor of Shlomo P. Neuman's 60th  
606 birthday. Geological Society of America, Special paper 348, p. 25–42.

607 Guan, J., F. J. Molz, Q. Zhou, H. H. Liu, and C. Zheng (2008), Behavior of the mass  
608 transfer coefficient during the MADE-2 experiment: New insights, *Water Resour. Res.*,  
609 44, W02423, doi:10.1029/2007WR006120.

610 Guting, N., A. Klotzsche, J. Van Der Kruk, J. Vanderborght, H. Vereecken, and A.  
611 Englert (2015), Spatially highly resolved mapping of aquifer heterogeneities using  
612 ground penetrating radar full-waveform tomography, AQUA 2015, 42<sup>nd</sup> IAH Congress,  
613 13-18 September 2015, Rome, Italy.

614 Hadley, P. W., and C. Newell (2014), The New Potential for Understanding Groundwater  
615 Contaminant Transport, *Groundwater*, 52, 174–186, doi: 10.1111/gwat.12135

616 Haggerty, R., S. W. Fleming, L. C. Meigs, and S. A. McKenna (2001), Tracer tests in a  
617 fractured dolomite: 2. Analysis of mass transfer in single-well injection-withdrawal  
618 tests, *Water Resour. Res.*, 37(5), 1129–1142, doi:10.1029/2000WR900334.

619 Harbaugh, A.W. (2005), MODFLOW-2005, The U.S. Geological Survey modular ground-  
620 water model—the Ground-Water Flow Process: U.S. Geological Survey Techniques  
621 and Methods 6-A16, variously p.

622 Harter, T. (2005), Finite-size scaling analysis of percolation in three-dimensional  
623 correlated binary Markov chain random fields. *Phys Rev E*, 72(2), 26120.  
624 doi:10.1103/PhysRevE.72.026120.

625 Harvey, C., and S. M. Gorelick (2000), Rate-limited mass transfer or macrodispersion:  
626 Which dominates plume evolution at the macrodispersion experiment (MADE) site?,  
627 *Water Resour. Res.*, 36(3), 637–650, doi:10.1029/1999WR900247.

628 Julian, H.E., J.M. Boggs, C. Zheng, and C.E. Feehley (2001) Numerical simulation of a  
629 natural gradient tracer experiment for the Natural Attenuation Study: flow and physical  
630 transport, *Groundwater*, 39(4), 534-545.

631 Klise, K. A., G. S. Weissmann, S. A. McKenna, E. M. Nichols, J. D. Frechette, T. F.  
632 Wawrzyniec, and V. C. Tidwell (2009), Exploring solute transport and streamline  
633 connectivity using lidar-based outcrop images and geostatistical representations of  
634 heterogeneity, *Water Resour. Res.*, 45, W05413, doi:10.1029/2008WR007500.

635 Koltermann, C. E., and S. M. Gorelick (1995), Fractional packing model for hydraulic  
636 conductivity derived from sediment mixtures, *Water Resour. Res.*, 31(12), 3283–3297,  
637 doi:10.1029/95WR02020.

638 Krumbein W.C. (1934), Size frequency distributions of sediments, *Journal of Sedimentary*  
639 *Petrology*, 4, 65–77.

640 LaBolle E.M., and G.E. Fogg (2001), Role of molecular diffusion in contaminant  
641 migration and recovery in an alluvial aquifer system, *Transport Porous Media*, 42 (1-  
642 2), 155–179.

643 Levy, M., and B. Berkowitz (2003), Measurement and analysis of non-Fickian dispersion  
644 in heterogeneous porous media, *J. Contam. Hydrol.*, 64, 203–226.

645 Lee S-Y., S.F. Carle, and G.E. Fogg (2007), Geologic heterogeneity and a comparison of  
646 two geostatistical models: Sequential Gaussian and transition probability-based  
647 geostatistical simulation, *Adv. Water Resour.*, 30, 1914–1932.

648 Liu, G., C. Zheng, and S. M. Gorelick (2004), Limits of applicability of the advection-  
649 dispersion model in aquifers containing connected high-conductivity channels, *Water*  
650 *Resour. Res.*, 40, W08308, doi:10.1029/2003WR002735.

651 Liu, G., C. Zheng, and S. M. Gorelick (2007), Evaluation of the applicability of the dual-  
652 domain mass transfer model in porous media containing connected high-conductivity  
653 channels, *Water Resour. Res.*, 43, W12407, doi:10.1029/2007WR005965.

654 Liu, G., J.J. Butler Jr., G.C. Bohling, E. Reboulet, S. Knobbe and D.W. Hyndman (2009),  
655 A new method for high-resolution characterization of hydraulic conductivity, *Water*  
656 *Resour. Res.*, 45, W08202, doi:10.1029/2009WR008319.

657 Liu, G., C. Zheng, G. R. Tick, J. J. Butler Jr., and S. M. Gorelick (2010), Relative  
658 importance of dispersion and rate-limited mass transfer in highly heterogeneous porous  
659 media: Analysis of a new tracer test at the Macrodispersion Experiment (MADE) site,  
660 *Water Resour. Res.*, 46, W03524, doi:10.1029/2009WR008430.

661 Llopis-Albert, C. and J.E. Capilla (2009), Gradual conditioning of non-Gaussian  
662 transmissivity fields to flow and mass transport data: 3. Application to the  
663 Macrodispersion Experiment (MADE-2) site, on Columbus Air Force Base in  
664 Mississippi (USA). *J. Hydrol.*, 371, 1-4, 75–84.

665 Meerschaert, M. M., M. Dogan, R. L. Van Dam, D. W. Hyndman, and D. A. Benson  
666 (2013), Hydraulic conductivity fields: Gaussian or not?, *Water Resour. Res.*, 49, 4730–  
667 4737, doi:10.1002/wrcr.20376.

668 Molz, F.J. (2015), Advection, dispersion, confusion, *Groundwater*, 53: 348–353. doi:  
669 10.1111/gwat.12338.

670 Neuman, S. P. (2014), The New Potential for Understanding Groundwater Contaminant  
671 Transport, *Groundwater*, 52, 653–656. doi: 10.1111/gwat.122

672 Neuman, S., Tartakovsky, D. (2009), Perspective on theories of non-fickian transport in  
673 heterogeneous media, *Adv. Water Resour.*, 32, 670–680 .

674 Odong J. (2007) Evaluation of empirical formulae for determination of hydraulic  
675 conductivity based on grain-size analysis, *J. Am. Sci.*, 3, 54–60.

676 Rehfeldt, K. R., J. M. Boggs, and L. W. Gelhar. 1992. Field study of dispersion in a  
677 heterogeneous aquifer 3. Geostatistical analysis of hydraulic conductivity, *Water*  
678 *Resour. Res.*, 28(12), 3309–3324.

679 Ritzi, R.W. (2000), Behavior of indicator variograms and transition probabilities in  
680 relation to the variance in lengths of hydrofacies, *Water Resour. Res.*, 36(11), 3375-  
681 3381.

682 Ritzi, R. W., Z. Dai, D.F. Dominic, and Y.N Rubin (2004), Spatial correlation of  
683 permeability in cross-stratified sediment with hierarchical architecture, *Water Resour.*  
684 *Res.*, 40(3), W03513, doi: 10.1029/2003WR002420.

685 Riva, M., L. Guadagnini, and A. Guadagnini (2010), Effects of uncertainty of lithofacies,  
686 conductivity and porosity distributions on stochastic interpretations of a field scale  
687 tracer test, *Stochastic. Environ. Res. Risk Assess.*, 24, 955–970, doi:10.1007/s00477-  
688 010-0399-7.

689 Ronayne, M. J., S. M. Gorelick, and C. Zheng (2010), Geological modeling of submeter  
690 scale heterogeneity and its influence on tracer transport in a fluvial aquifer, *Water*  
691 *Resour. Res.*, 46, W10519, doi:10.1029/2010WR009348.

692 Salamon, P., D. Fernandez-Garcia, and J. J. Gómez-Hernández (2007), Modeling tracer  
693 transport at the MADE site: The importance of heterogeneity, *Water Resour. Res.*, 43,  
694 W08404, doi:10.1029/2006WR005522.

695 Seiler, K.-P. (1973), Durchlässigkeit, Porosität und Kornverteilung quartärer Kies-Sand-  
696 Ablagerungen des bayrischen Alpenvorlandes, Gas- und Wasserfach - Wasser,  
697 Abwasser – 114. Jahrgang, Heft 8, S. 353-358.

698 Silliman, S. E., L. F. Konikow, and C. I. Voss (1987), Laboratory investigation of  
699 longitudinal dispersion in anisotropic porous media, *Water Resour. Res.*, 23(11), 2145–  
700 2151, doi:10.1029/WR023i011p02145.

701 Srinivasan, G., D.M. Tartakovsky, M. Dentz, H. Viswanathan, B. Berkowitz, and B.A.  
702 Robinson (2010), Random walk particle tracking simulations of non-Fickian transport  
703 in heterogeneous media, *Journal of Computational Physics*, 229(11), 4304-4314.

704 Stauffer, T. B., C. P. Antworth, R. G. Young, W. G. MacIntyre, J. M. Boggs, and L. M.  
705 Beard (1994), Degradation of aromatic hydrocarbons in an aquifer during a field  
706 experiment demonstrating the feasibility of remediation by natural attenuation, Rep.  
707 AL/EQ TR 1993-0007, Armstrong Lab., Tyndall Air Force Base, Fla.

708 Vukovic´ M, Soro A (1992) Hydraulics and water wells: theory and application. Water  
709 Resources Publications, Highlands Ranch, CO, USA. 1143 Hydrogeology.

710 Webb, E. K., and M. P. Anderson (1996), Simulation of Preferential Flow in Three-  
711 Dimensional, Heterogeneous Conductivity Fields with Realistic Internal Architecture,  
712 *Water Resour. Res.*, 32(3), 533–545, doi:10.1029/95WR03399.

713 Weissmann, G.S., S.F. Carle and G.E. Fogg, 1999, Three-dimensional hydrofacies  
714 modeling based on soil surveys and transition probability geostatistics, *Water Resour.*  
715 *Res.*, 35(6), 1761-1770.

716 Ye, M., and R. Khaleel (2008), A Markov chain model for characterizing medium  
717 heterogeneity and sediment layering structure, *Water Resour. Res.*, 44, W09427,  
718 doi:10.1029/2008WR006924.

719 Zhang, Y., C. Green, and G. Fogg (2013), The impact of medium architecture of alluvial  
720 settings on non-fickian transport, *Adv. Water Resour.*, 54, 78–99.

721 Zhang, Y., and D. A. Benson (2008), Lagrangian simulation of multidimensional  
722 anomalous transport at the MADE site, *Geophys. Res. Lett.*, 35, L07403,  
723 doi:10.1029/2008GL033222.

724 Zheng, C., and S. M. Gorelick (2003), Analysis of the effect of decimeter scale  
725 preferential flow paths on solute transport, *Groundwater*, 41(2), 142– 155.

726 Zheng, C. (2010), MT3DMS v5.3 Supplemental User’s Guide, Technical Report,  
727 Department of Geological Sciences, University of Alabama, Tuscaloosa, Alabama.

728 Zheng, C., M. Bianchi, and S.M. Gorelick (2011), Lessons learned from 25 years of  
729 research at the MADE site, *Groundwater*, 49, 649–662, doi:10.1111/j.1745–  
730 6584.2010.00753.x.

731

732 **LIST OF TABLES**

733

734 Table1. Criteria used for lithofacies identification and representative parameters.

|                                  | Highly<br>conductive<br>gravel<br>(HCG)                                  | Gravel with<br>sand<br>(GS) | Sand gravel<br>and fines<br>(SGf) | Sand and<br>gravel<br>(SG) | Well sorted<br>sand<br>(S) |
|----------------------------------|--------------------------------------------------------------------------|-----------------------------|-----------------------------------|----------------------------|----------------------------|
| Identification criteria          | G > 50%<br>f < 5%<br>d <sub>10</sub> > 0.25 mm<br>d <sub>25</sub> > 1 mm | G > 50%<br>f < 5%           | f > 5%                            | S > 50%<br>f < 5%          | S > 85%<br>U < 3           |
| G* [%]                           | 64.6                                                                     | 56.2                        | 40.8                              | 32.2                       | 3.1                        |
| S* [%]                           | 32.0                                                                     | 40.7                        | 51.7                              | 64.9                       | 90.2                       |
| f* [%]                           | 3.4                                                                      | 3.1                         | 7.5                               | 2.9                        | 6.7                        |
| d <sub>10</sub> * [mm]           | 0.62                                                                     | 0.22                        | 0.14                              | 0.21                       | 0.12                       |
| d <sub>25</sub> * [mm]           | 2.7                                                                      | 0.72                        | 0.45                              | 0.36                       | 0.16                       |
| d <sub>60</sub> * [mm]           | 12.4                                                                     | 8.73                        | 5.56                              | 3.3                        | 0.28                       |
| U*                               | 30.4                                                                     | 41.0                        | 38.3                              | 15.6                       | 2.6                        |
| Proportions [%]                  | 12                                                                       | 18                          | 35                                | 14                         | 21                         |
| Mean length [m]                  | 30                                                                       | 31                          | 39                                | 25                         | 35                         |
| Mean thickness [m]               | 1.0                                                                      | 0.5                         | 0.9                               | 0.4                        | 1.7                        |
| Mean Log <sub>10</sub> (K) [m/d] | 2.482                                                                    | 0.830                       | 0.402                             | 0.889                      | 0.752                      |
| Variance Log <sub>10</sub> (K)   | 0.589                                                                    | 0.210                       | 0.343                             | 0.228                      | 0.165                      |
| Mean $\theta$                    | 0.265                                                                    | 0.257                       | 0.259                             | 0.298                      | 0.415                      |

735

736 G: gravel content;

737 S: sand content;

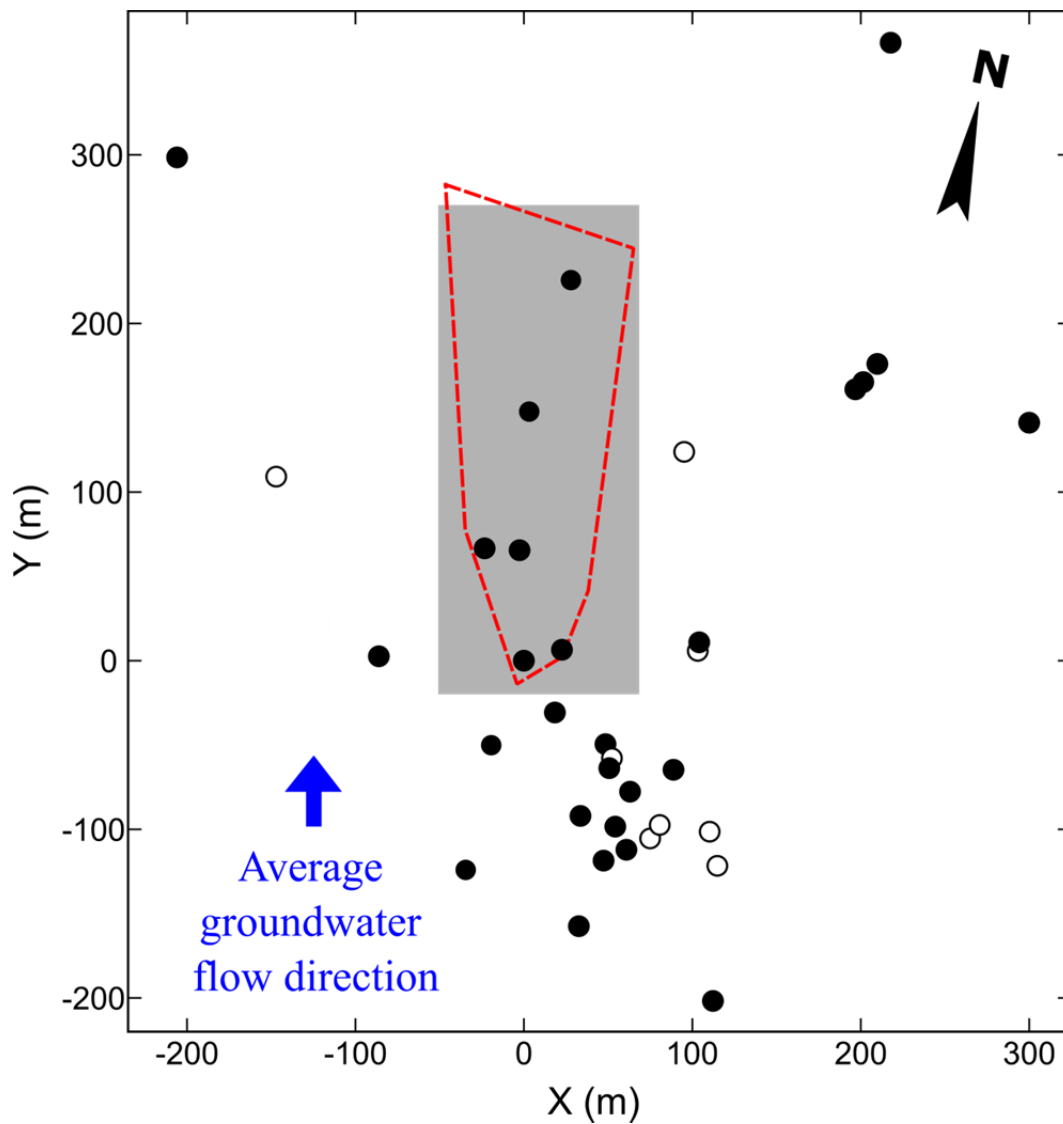
738 f: fines content

739 \* average value

740

741 LIST OF FIGURES

742



743

744

745 Figure 1. Map of boreholes used for lithological characterization of the MADE site. Black

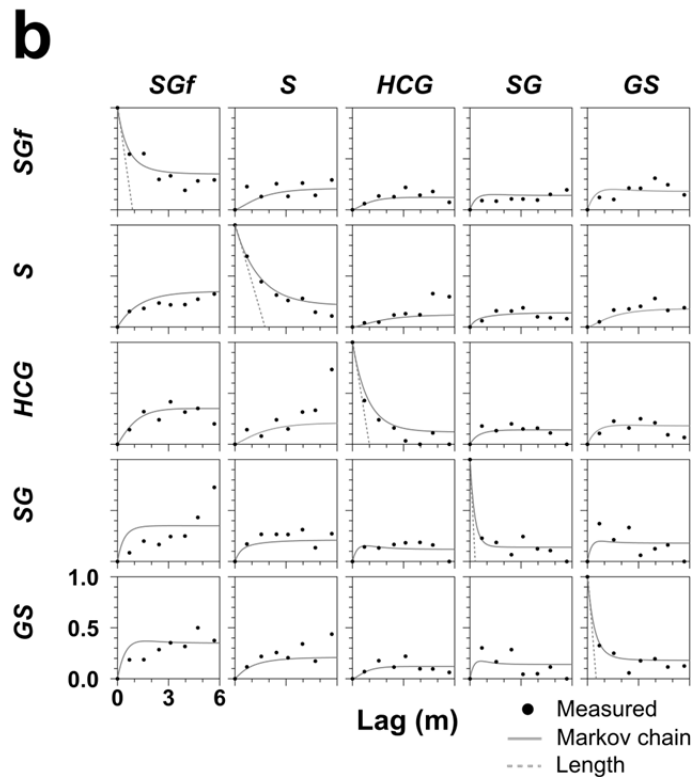
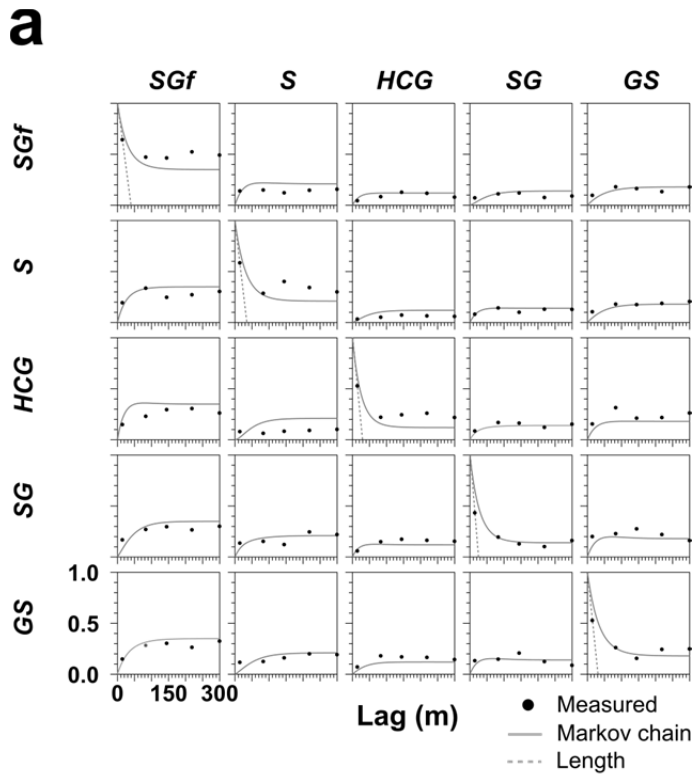
746 circles indicate boreholes with grain size data in Appendix A in *Boggs et al.* [1990].

747 Boreholes with only lithological description are indicated by open circles. The grey

748 shaded area indicates the extension of the domain used for flow and transport modelling.

749 The red dashed line indicates the boundary of the network of multilevel sampling wells

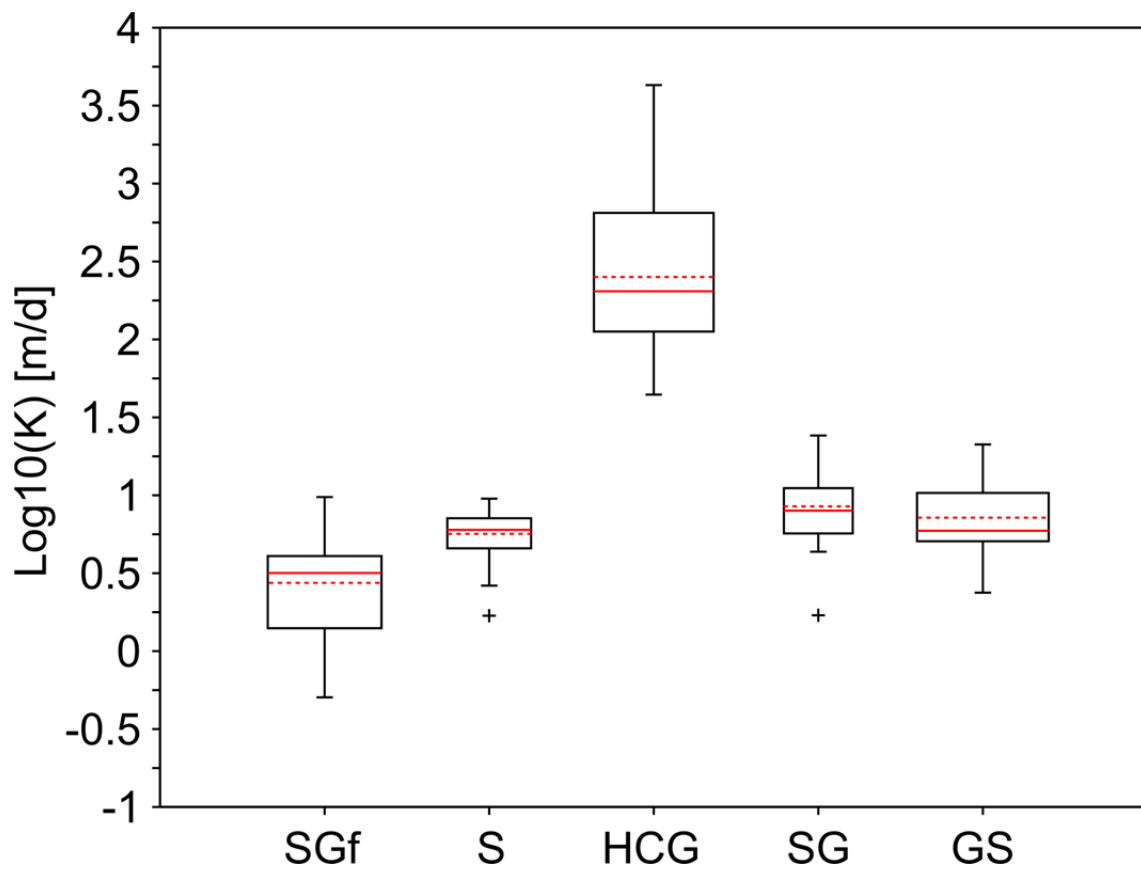
750 used during the large-scale tracer tests.



751

752 Figure 2. Lateral (a) and vertical (b) transition probabilities and fitted Markov chain

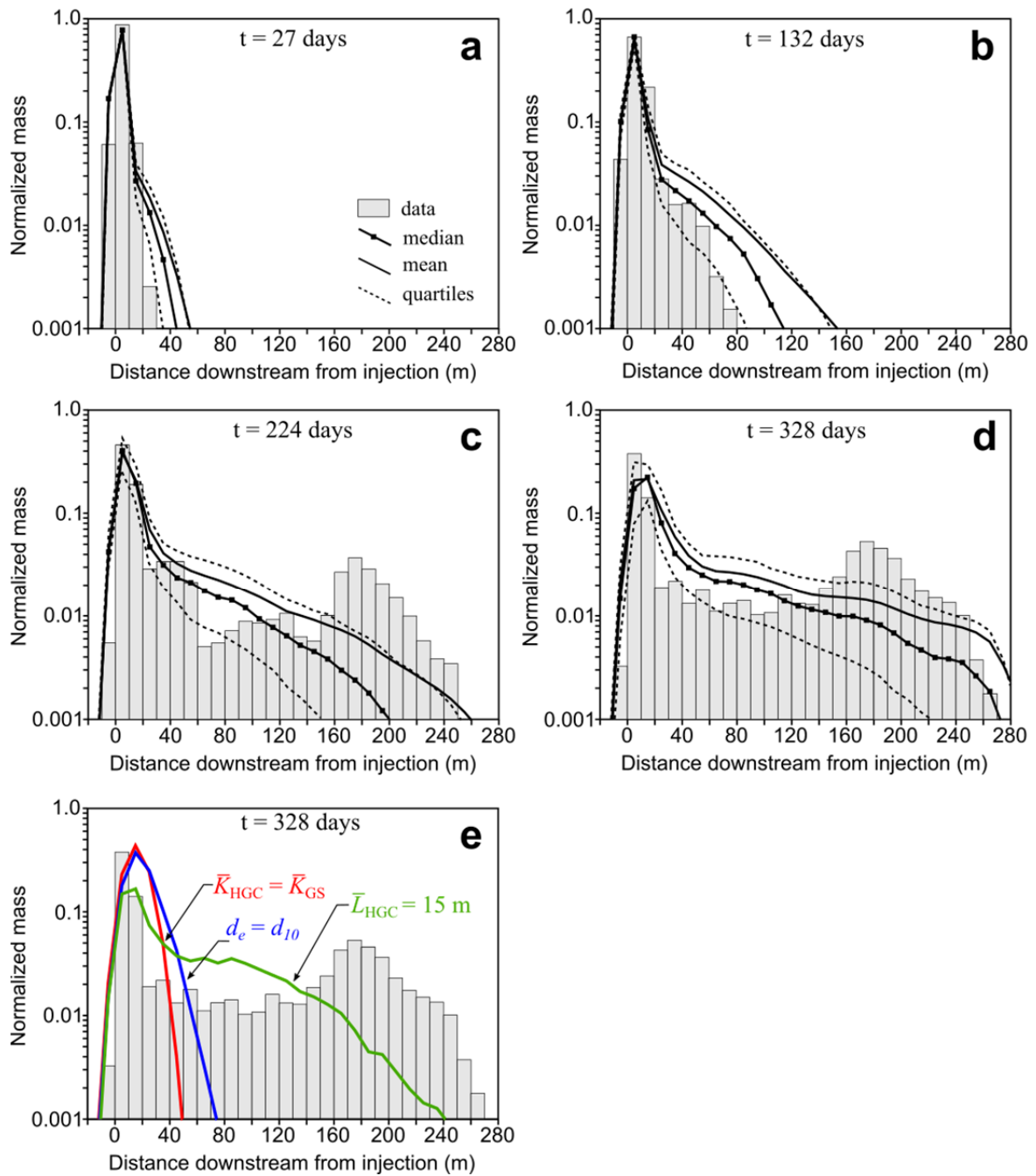
753 model.



754

755

756 Figure 3. Box plots of the estimated log-transformed hydraulic conductivity (K) values for  
 757 each lithofacies showing median, interquartile range and extreme values (crosses). Red  
 758 dashed lines indicate mean values.

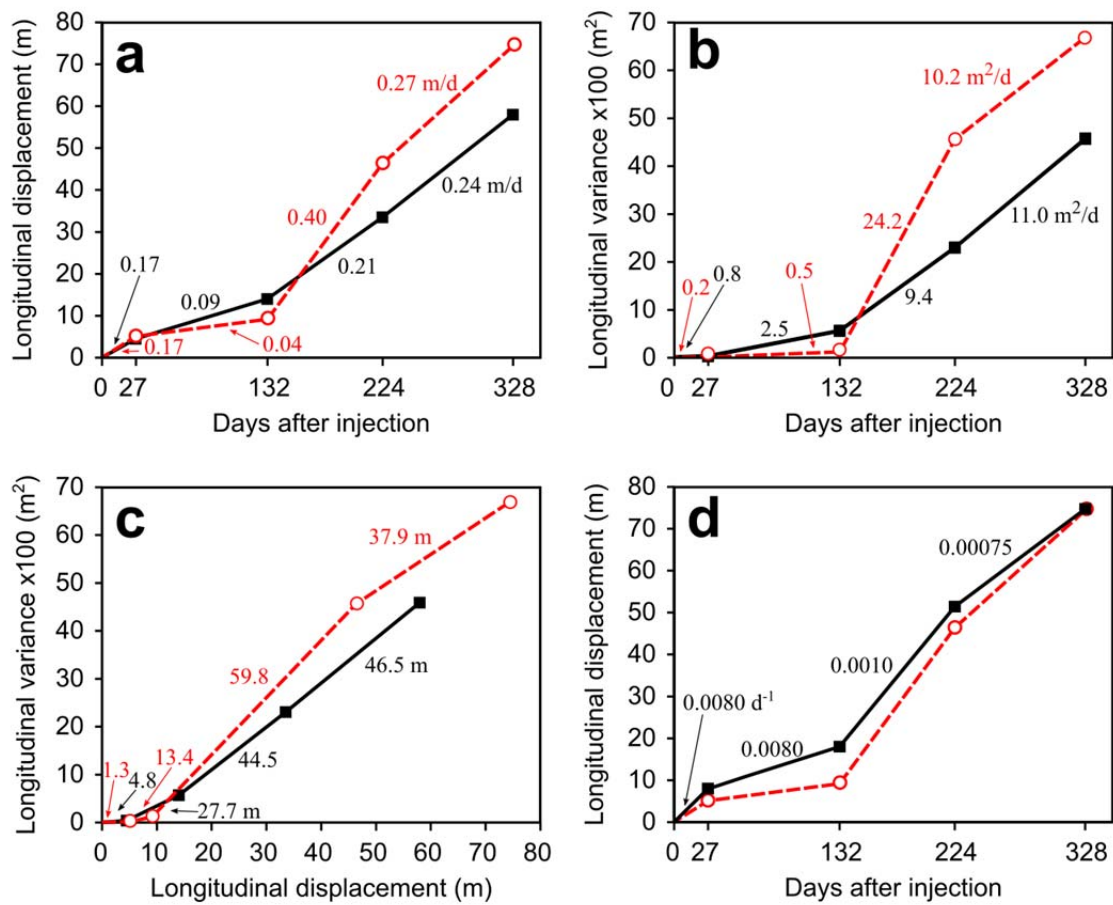


759

760

761 Figure 4. (a-d) Observed and simulated longitudinal mass distributions of the tritium  
 762 plume. Simulated distributions were obtained with input parameters in Table 1. (e) Mass  
 763 distribution at 328 days for simulations considering different mean  $K$  and mean length for  
 764 lithofacies HCG. The scenario assuming a mean  $K$  value for HGC equal to that for

765 lithofacies GS is shown red. The scenario assuming  $d_e$  as  $d_{10}$  for  $K$  estimations is shown in  
766 blue. The scenario assuming a mean length ( $\bar{L}$ ) of 15 m is shown in green.  
767



768

769

770 Figure 5. First and second central spatial moments evolution for the observed (in red) and

771 simulated (in black) plumes. Simulated points in a-c represent mean values of the Monte

772 Carlo realizations. (a) Values indicate the estimated mean plume velocity. (b) Values

773 indicate one half of the growth rate of the longitudinal variance with time (c) Values

774 indicate one half of growth rate of the longitudinal variance with the mean travel distance.

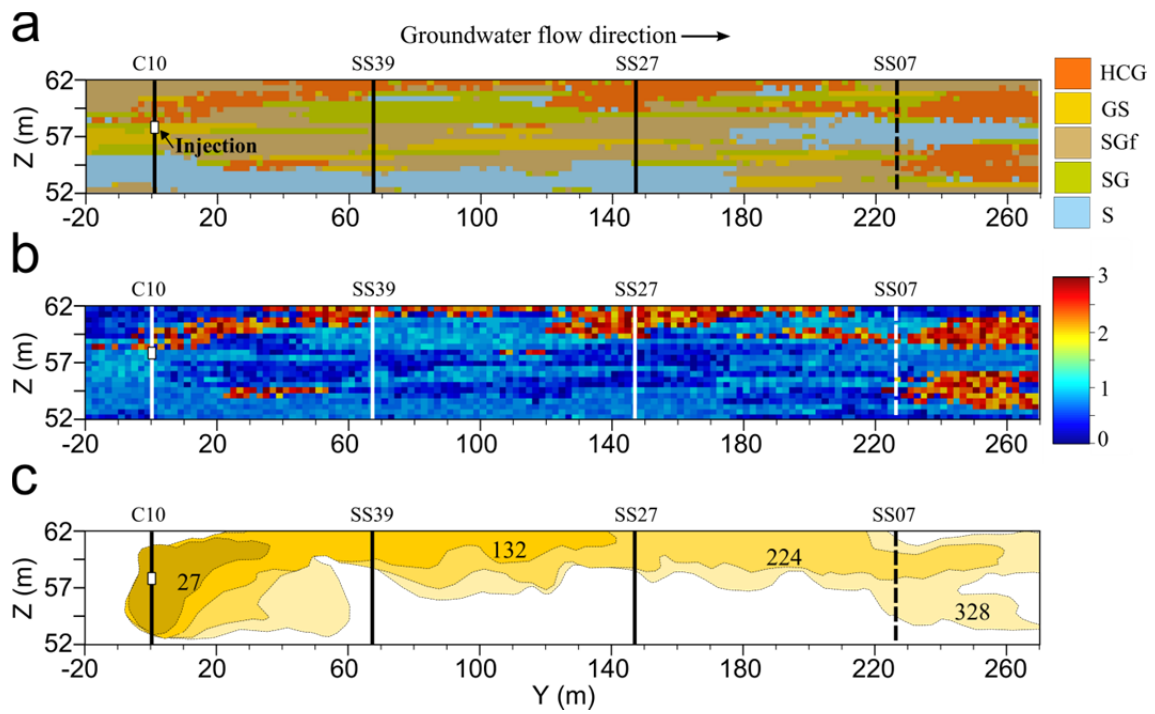
775 Under the assumption of a uniform flow field these values correspond to the macroscopic

776 longitudinal dispersivity. (d) Longitudinal displacement of a dual-domain single rate mass

777 transfer model (DDM) in which the ratio of mobile to total porosity is equal to the

778 volumetric fraction of HCG. Values indicate calibrated values for the mass transfer rate

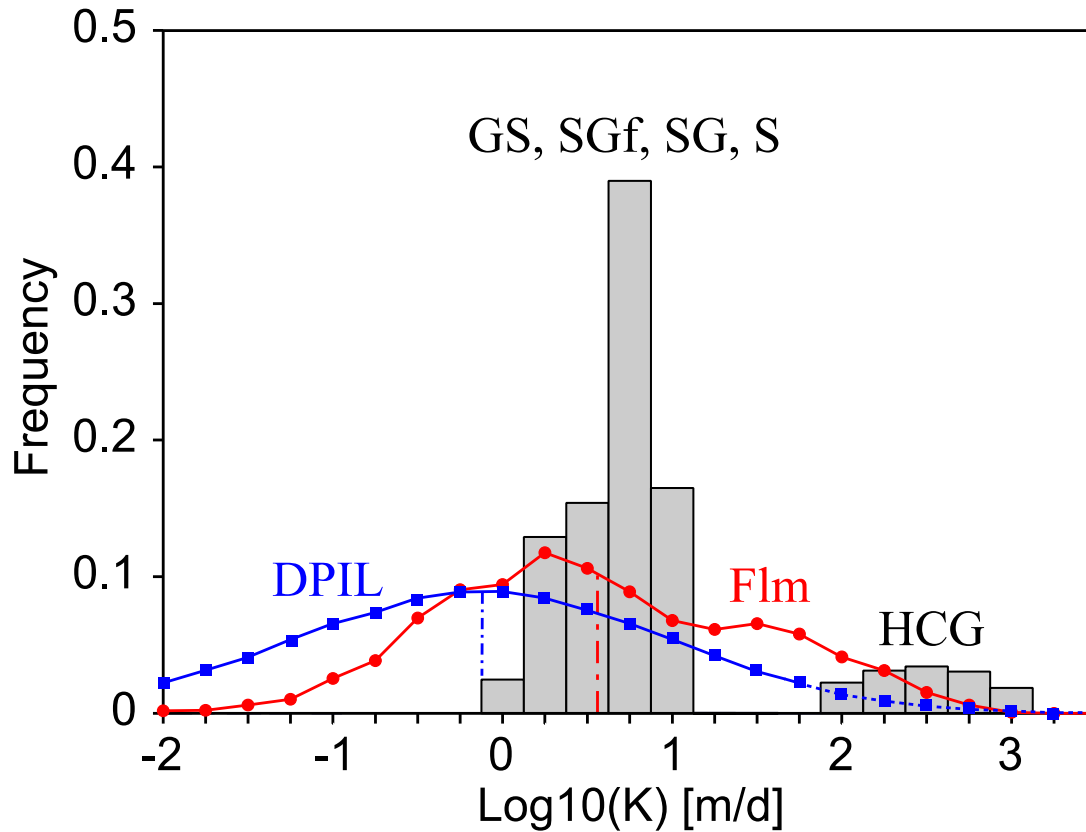
779 coefficient (see text for explanation).



780

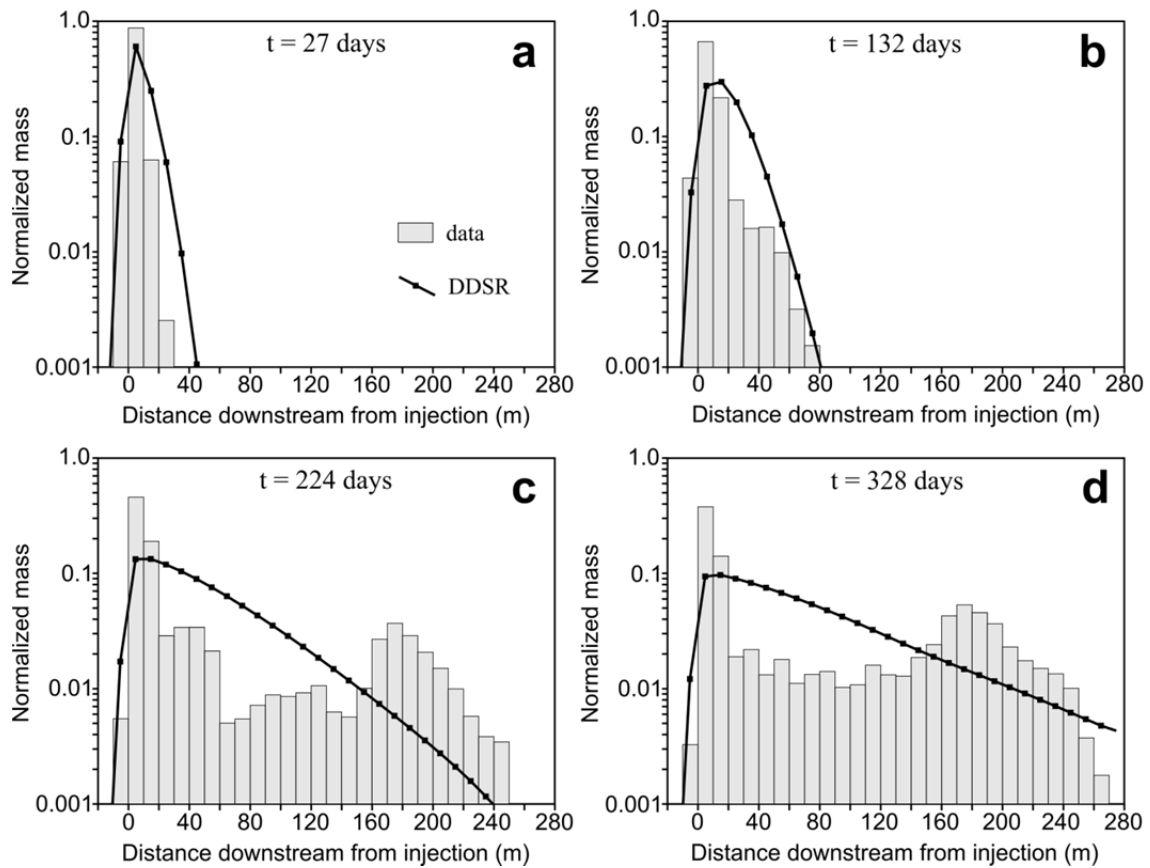
781

782 Figure 6. (a) One equally probable realization of the simulated spatial distribution of  
 783 lithofacies shown in a cross section oriented parallel to the main flow direction and  
 784 crossing through the injection site and three boreholes. Location of borehole SS07 is  
 785 projected. (b) Corresponding  $\log_{10}(K)$  field [m/d]. (c) Evolution of the simulated plume  
 786 front ( $C = 2\text{pCi/ml}$ ) with time.



787

788 Figure 7. Example of frequency distribution of the generated  $K$  fields. The distributions of  
 789 the  $K$  measurements using the impeller flowmeter (Flm) and direct-push injection logger  
 790 (DPIL) are also shown. The vertical dash-dot lines indicate the mean of the two  
 791 distributions. Flowmeter measurements data from *Rehfeldt et al.* [1992]. The DPIL data  
 792 distribution was estimated by assuming a lognormal distribution with a geometric mean of  
 793  $8.9 \times 10^{-6}$  m/s and a variance of natural log-transformed  $K$  values of 6.6 [Table 1 in *Bowling*  
 794 *et al.*, 2012]. The upper limit of the DPIL instrument is about 60 m/d [*Bowling et al.*,  
 795 2012; *Dogan et al.*, 2014].



796

797

798 Figure 8. Observed and simulated longitudinal mass distributions of the tritium plume.

799 Simulated profiles were calculated with a dual-domain single rate mass transfer model in

800 which the ratio of mobile to total porosity is equal to the volumetric fraction of HCG.

801 Values for the mass transfer rate coefficient (see Figure 5d) were estimated by calibration

802 with a trial-and-error approach.